Iterative modal reconstruction for sparse particle tracking data

Grille Guerra, Adrian; Sciacchitano, Andrea; Scarano, Fulvio

Citation (APA)
Grille Guerra, A., Sciacchitano, A., & Scarano, F. (2024). Iterative modal reconstruction for sparse particle tracking data. *Physics of Fluids*, *36*(7), Article 075107. https://doi.org/10.1063/5.0209527

Important note
To cite this publication, please use the final published version (if applicable).
Please check the document version above.

Iterative modal reconstruction for sparse particle tracking data

Adrian Grille Guerra ✉ iD ; Andrea Sciacchitano iD ; Fulvio Scarano iD

Check for updates

View Online

Export Citation

Physics of Fluids

Special Topic:
Recent Advances in Fluid Dynamics and its Applications

Guest Editors: B.Reddappa, B. Rushi Kumar, Sreedhara Rao Gunakala, Bijula Prabhakar Reddy

Submit Today!

AIP Publishing

Iterative modal reconstruction for sparse particle tracking data

View Online   Export Citation   CrossMark

Adrian Grille Guerra,[a] ⓘD Andrea Sciacchitano, ⓘD and Fulvio Scarano ⓘD

AFFILIATIONS

Delft University of Technology, Faculty of Aerospace Engineering, Delft, The Netherlands

[a]Author to whom correspondence should be addressed: a.grilleguerra@tudelft.nl

ABSTRACT

A method to reconstruct the dense velocity field from relatively sparse particle tracks is introduced. The approach leverages the properties of proper orthogonal decomposition (POD), and it iteratively reconstructs the detailed spatial modes from a first, coarse estimation thereof. The initially coarse Cartesian representation of the velocity field is obtained by local data averaging, where POD is applied. The spatial resolution of the POD modes is enhanced by reprojecting them onto the sparse particle velocity to iteratively improve the reconstruction of the temporal coefficients. Finally, the enhanced velocity field is represented at high-resolution with a reduced order model using the dominant POD modes. The method is referred to as iterative modal reconstruction (IMR), as an extension of the recently proposed data-enhanced particle tracking velocimetry algorithm, introduced for cross correlation-based velocity data. Experiments in the wake of a cylinder at $Re_D = 27\,000$ are used to assess the suitability of the method to resolve the turbulent Kármán–Benard wake. The approach is benchmarked against traditional as well as state-of-the-art reconstruction methods, illustrating the capability of IMR of enhancing the spatial resolution of sparse velocity data.

I. INTRODUCTION

Lagrangian Particle Tracking (LPT) is an established measurement method for three-dimensional flow diagnostics (Schröder and Schanz, 2023), superseding traditional tomographic PIV (Elsinga *et al.*, 2006) in terms of computational efficiency and spatial resolution. In particular, the Shake-the-Box algorithm (Schanz *et al.*, 2016) is now considered the state-of-the-art method for data analysis, yielding a multitude of velocity vectors obtained, tracking the particle tracers dispersed in the flow. Cartesian grid data reduction (CGR) is a convenient operation to support data inspection as well as for evaluating derivatives (e.g., vorticity and shear rate) or integrals, like velocity circulation and pressure (van Oudheusden, 2013). While ensemble-averaging of pointwise properties can be achieved at the desired spatial resolution by increasing the length of the measurement series (Agüera *et al.*, 2016, among others), the evaluation of the instantaneous flow structures as well as the turbulent vorticity fluctuations are strongly dependent upon the tracer concentration. For instantaneous measurements, averaging tracks over small regions leads to gappy velocity fields, requiring refill operations like interpolation or Kriging regression (de Baar *et al.*, 2014). More complex data assimilation methods have been proposed, namely, the VIC+ (Schneiders and Scarano, 2016) and

FlowFit (Gesemann, 2016) techniques, which reduce the constraint imposed on particle concentration. Such methods fit the experimental data and enforce the governing equations of fluid motion.

While most of the data assimilation approaches employ solely the instantaneous velocity and acceleration for CGR purposes, recent works are proposing the use of a finite temporal segment (i.e., 4D data assimilation). Within the framework of the vortex-in-cell (VIC) technique (Schneiders *et al.*, 2014), time-segment assimilation, using advection-based models (Jeon *et al.*, 2019) or vorticity transport (Scarano *et al.*, 2022), has proven effective.

Beyond the use of time segments for CGR, Cortina-Fernández *et al.* (2021) approached the problem invoking the proper orthogonal decomposition (POD) method. The data-enhanced particle tracking velocimetry (DEPTV) exploits the statistical properties of full sequence of measured snapshots. Borrowing ideas from gappy POD approaches (Raben *et al.*, 2012; Venturi and Karniadakis, 2004) that aim at filling the gaps of cross correlation PIV measurements, the DEPTV method combines a modal decomposition of gridded data (from cross correlation analysis of PIV images) and particle tracking information (from the same set of images) to provide a CGR of the particle tracks at an increased spatial resolution. The modal decomposition obtained from

cross correlation data is employed to generate a temporal basis on which to project the particle tracks, thus providing a representation of the spatial POD modes at increased resolution. While initially developed for planar 2D PIV data, the approach has been recently extended to 3D tomographic-PIV experimental data (Tirelli *et al.*, 2023).

The inherent limitation of DEPTV stems from the representation of the temporal coefficients. Since the temporal basis arises from low-resolution cross correlation analysis, only flow features that are partially resolved by it can be enhanced with DEPTV. This can be overcome with the use of a predictor–corrector iterative approach, where the temporal basis is updated by reprojecting the particle trajectories onto the high-resolution spatial basis. The process may be repeated until convergence of the decomposition.

The present work leverages on the concepts introduced by the DEPTV method to achieve dense velocity reconstruction for relatively sparse data measured with particle tracking. In the present approach, the spatiotemporal modal decomposition is enhanced iteratively, aiming at super-resolution, i.e., the reconstructed velocity field estimates flow features beyond the average inter-particle distance of the original data. The new method is referred to as iterative modal reconstruction (IMR), and its algorithm is presented in Sec. II. The performance of the method is evaluated from the analysis of experimental LPT data obtained with large-scale PIV measurements in the wake of a cylinder at $Re_D = 27\,000$ (Sec. III). Finally, a comparative analysis is performed, benchmarking IMR against DEPTV and the effects of the iterative approach are discussed. Additionally, IMR is compared to linear interpolation and physics-based VIC data assimilation. The results quantify the measurement error of IMR using the downsampling/resampling technique to provide an experimental ground truth. Furthermore, the spatial resolution of the resulting CGR is evaluated by inspection of the coherent vortical structures in the cylinder wake in relation to other observations from the literature. The final part of the work discusses the requirements for statistical convergence of IMR to provide a criterion for real-world experiments.

II. THE IMR METHOD

The input to the IMR method is a relatively long sequence of LPT data obtained with a coarse resolution, which is initially transformed onto a Cartesian grid as discussed in Sec. II A. The gridded data undergoes an iterative modal decomposition procedure, as described in Sec.

II B, which is used to build a reduced order model (ROM) of the instantaneous velocity field at high spatial resolution, as discussed in Sec. II C. The computational complexity of the method is presented in Sec. II D, together with an overview of the algorithm.

A. CGR of LPT data

Consider the set of particle trajectories obtained by LPT measurements, as sketched in the left part of Fig. 1, and represented by scattered velocity vectors at the particles' locations. In the time domain, n_{time} snapshots are acquired at a sampling frequency f_{acq}. The sparse velocity vectors are initially projected onto a coarse Cartesian grid (see Fig. 1) of spacing h_{LR} through window-based averaging (i.e., binning) to avoid data gaps (bins without velocity information) and prevent biasing the modal decomposition toward regions of higher seeding concentration. This is relevant, but not restricted to, for large-scale PIV experiments involving the use of helium-filled soap bubbles (HFSB) as tracers (Bosbach *et al.*, 2009). As a rule of thumb, for an average inter-particle distance $\bar{r}$, the bin size may be conservatively chosen one order of magnitude larger than $\bar{r}$. This choice ensures that bins include at least a few datapoints in regions of lower seeding concentration.

Each snapshot of the binned data may be reshaped into a row vector $\boldsymbol{u}_{LR_k} \in \mathbb{R}^{1 \times n_s^{LR}}$, with n_s^{LR} representing the total number of spatial elements, this is, $n_s^{LR} = 3 n_x n_y n_z$ after accounting for the three velocity components. Appending all vectors returns the low-resolution velocity data matrix $\boldsymbol{U}_{LR} \in \mathbb{R}^{n_{time} \times n_s^{LR}}$.

IMR is intended for statistically stationary processes, with the modal analysis targeting the fluctuating component of the velocity field only, $\boldsymbol{u}'_{LR_k} \in \mathbb{R}^{1 \times n_s^{LR}}$, obtained via Reynolds decomposition as $\boldsymbol{u}'_{LR_k} = \boldsymbol{u}_{LR_k} - \bar{\boldsymbol{u}}_{LR}$, where $\bar{\boldsymbol{u}}_{LR} \in \mathbb{R}^{1 \times n_s^{LR}}$ is the time-averaged velocity field. The extension of the method to non-stationary processes is out of the scope of the current work. The vectors of velocity fluctuations are reshaped into a low-resolution fluctuating velocity data matrix $\boldsymbol{U}'_{LR} \in \mathbb{R}^{n_{time} \times n_s^{LR}}$.

In parallel, the scattered velocity vectors at the particles' locations are projected onto a finer Cartesian grid, as sketched in Fig. 2, of spacing h_{HR} (and n_s^{HR} spatial elements), with $h_{HR} < h_{LR}$, through a similar binning process. The value of h_{HR} is chosen according to the statistical convergence of the ensemble of snapshots, as will be discussed in the
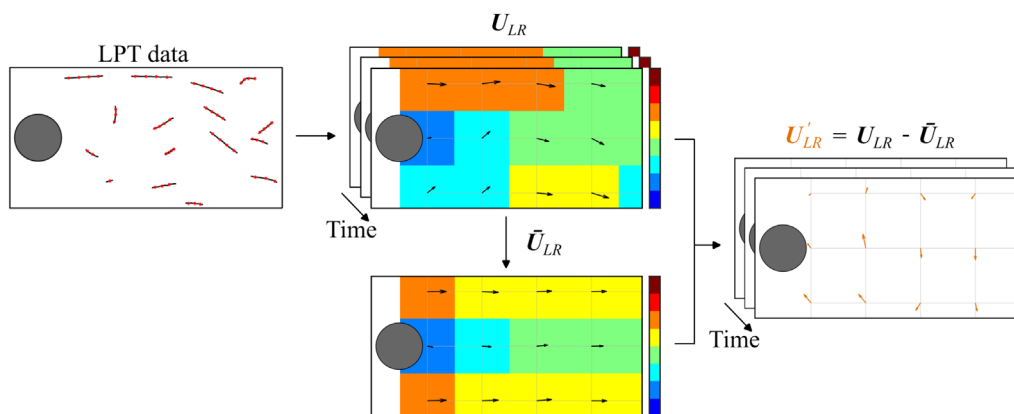
FIG. 1. Sketch of the low-resolution velocity field, $\boldsymbol{U}_{LR}$, obtained from the LPT data, and the corresponding fluctuating component, $\boldsymbol{U}'_{LR}$, obtained via Reynolds decomposition.
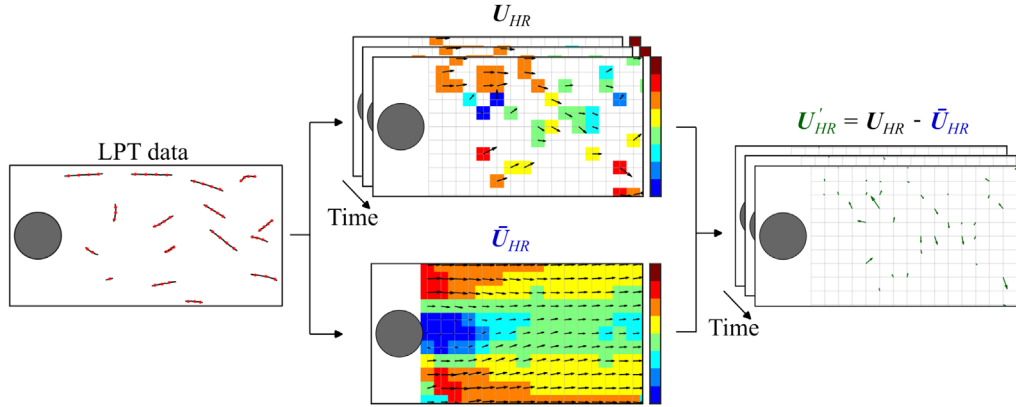
FIG. 2. Sketch of the high-resolution (gappy) velocity field, U_{HR}, the time-averaged flow field obtained from ensemble-averaging of the particle tracks, $\bar{U}_{HR}$, and the fluctuating part U'_{HR}.

remainder of the document. Because of the relatively small size of the bins used in the high-resolution Cartesian grid, the resulting velocity field, rearranged as $U_{HR} \in \mathbb{R}^{n_{time} \times n_s^{HR}}$, will contain gaps that do not contribute to the modal reconstruction process. The time-averaged velocity field at this spatial resolution, $\bar{u}_{HR} \in \mathbb{R}^{1 \times n_s^{HR}}$, can be obtained from an ensemble particle tracking approach (Cowen and Monismith, 1997; Kähler *et al.*, 2012) instead of Reynolds decomposition for improved accuracy (Tirelli *et al.*, 2023). The row vector $\bar{u}_{HR}$ can be stacked to form a data matrix $\bar{U}_{HR} \in \mathbb{R}^{n_{time} \times n_s^{HR}}$ and obtain the high resolution fluctuating velocity matrix $U'_{HR} \in \mathbb{R}^{n_{time} \times n_s^{HR}}$ as $U'_{HR} = U_{HR} - \bar{U}_{HR}$.

B. Iterative modal decomposition

The low resolution CGR operation is employed to construct an initial guess of the modal decomposition of the dataset, as illustrated in Fig. 3, unaffected by the presence of gaps in the binned velocity representation. As in the original implementation of the DEPTV method, the spatiotemporal bases are obtained from POD, but other decomposition choices are also possible (see, for instance, the work of Mendez *et al.*, 2019). The POD decomposition of U'_{LR}, which can be implemented via the singular value decomposition (SVD) of the data matrix, reads

$$U'_{LR} = \Psi_0 \Sigma_0 \Phi_0^T, \qquad (1)$$

where $\Psi_0 = \left[\psi_1, \ldots, \psi_{rk(U'_{LR})} \right] \in \mathbb{R}^{n_{time} \times rk(U'_{LR})}$ and $\Phi_0 = [\phi_1, \ldots, \phi_{rk(U'_{LR})}] \in \mathbb{R}^{n_s^{LR} \times rk(U'_{LR})}$ are the orthonormal matrices that contain the so-called temporal (chronos) and spatial (topos) modes, respectively. $\Sigma_0 = \text{diag}[\sigma_1, \ldots, \sigma_{rk(U'_{LR})}] \in \mathbb{R}^{rk(U'_{LR}) \times rk(U'_{LR})}$ is the diagonal matrix containing the energy contribution of each mode, which for the case of velocity fluctuations represents the turbulent kinetic energy content. The total number of modes is dictated by the rank of the data matrix, $rk(U'_{LR}) = \min(n_{time}, n_s^{LR})$. The common choice of POD is a result of the optimality of the decomposition from an energy perspective (using the L^2 error), as guaranteed by the Eckart–Young–Mirsky theorem (Eckart and Young, 1936).

The initial guess of the temporal basis is employed to increase the spatial resolution of the spatial modes (see Fig. 3), from the grid spacing h_{LR} to h_{HR} in an iterative manner, denoted by the subscript $_n$. This is achieved by projecting Ψ_0 (represented as Ψ_{n-1} in the iterative process) onto the high resolution fluctuating velocity data matrix, thus creating an updated representation of the spatial modes in a similar fashion to the extended POD modes discussed by Borée (2003). To account for the sparsity of U'_{HR}, the projection step must be normalized to compensate for changes in seeding concentration across the measurement volume. For every spatial bin (or column of U'_{HR}), counting the number of velocity entries is used to construct a vector of temporal occurrences, $n_t \in \mathbb{R}^{1 \times n_s^{HR}}$. After normalizing by the total number of snapshots n_{time}, as $\hat{n}_t = n_t / n_{time}$, this information can be stacked to generate the matrix of temporal occurrences $\hat{N}_t \in \mathbb{R}^{rk(U'_{LR}) \times n_s^{HR}}$, which leverages the projection operator. Taking this into account, the projection of the temporal basis onto U'_{HR} returns

$$\Sigma_n \Phi_n^T = \left(\Psi_{n-1}^T U'_{HR} \right) \oslash \hat{N}_t, \qquad (2)$$

where $\oslash$ denotes the Hadamard (element-wise) division operator. Inspection of Eq. (2) reveals that the spatial resolution of $\Phi_n \in \mathbb{R}^{n_s^{HR} \times rk(U'_{LR})}$ has been increased according to the grid spacing h_{HR}. The updated POD modes may be sorted according to their new energy contribution, $\Sigma_n \in \mathbb{R}^{rk(U'_{LR}) \times rk(U'_{LR})}$, and the minor loss of orthogonality introduced in the projection step is corrected via reduced QR factorization of Φ_n.

While in the DEPTV method the high-resolution spatial modes are combined with the initial guess of the temporal coefficients to reconstruct the instantaneous velocity field, IMR uses Φ_n to further update the temporal modes, and the process is repeated until convergence of the decomposition. This is achieved by reprojecting Φ_n onto U'_{HR}, after accounting for the spatial sparsity of the snapshots. In an analogous fashion, for every snapshot (or row of U'_{HR}), counting the number of velocity entries is used to construct a vector of spatial occurrences, $n_s \in \mathbb{R}^{n_{time} \times 1}$. After normalizing by the total number of spatial elements, as $\hat{n}_s = n_s / n_s^{HR}$, this information can be stacked to generate the matrix of spatial occurrences $\hat{N}_s \in \mathbb{R}^{n_{time} \times rk(U'_{LR})}$. This matrix accounts for the changes in particles' concentration along time, which
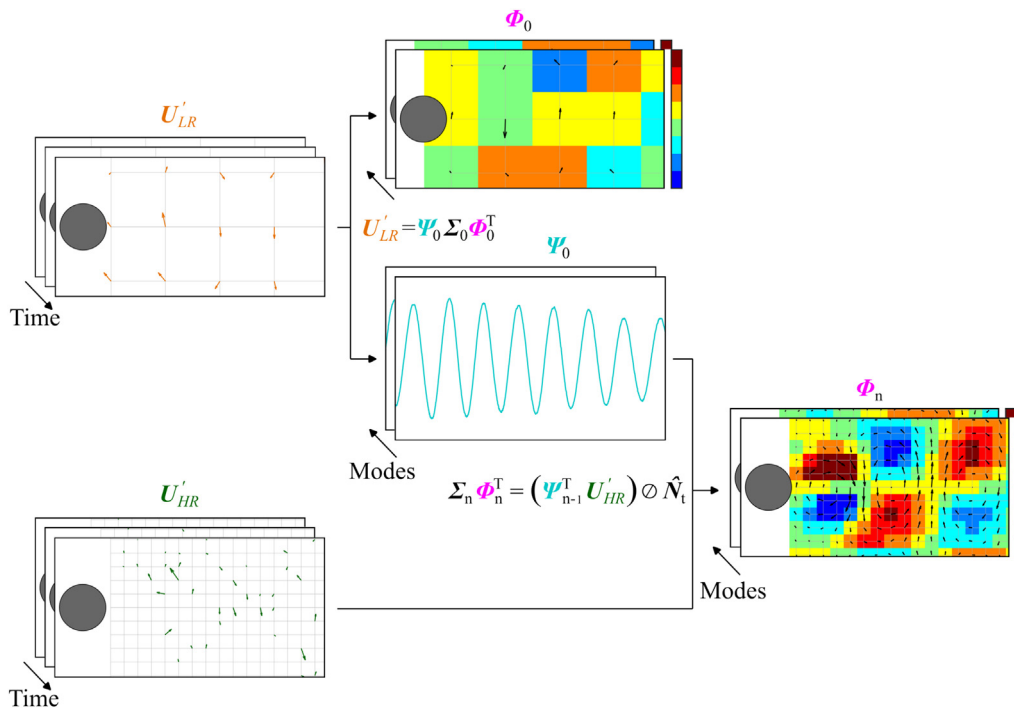
FIG. 3. Sketch of the initial POD decomposition from the coarse binning data U'_{LR}, and projection of the temporal coefficients Ψ onto the high resolution (gappy) velocity field U'_{HR} to increase the spatial resolution of the spatial modes Φ.

is usually rather minor compared to the changes across space. Including this contribution, the reprojection step reads

$$\Psi_n = \left(U'_{HR}\Phi_n\Sigma_n^{-1}\right) \oslash \widehat{N}_s. \tag{3}$$

The process is completed by restoring the orthogonality of Ψ_n via reduced QR factorization and by checking the convergence of the process. The latter is implemented by requiring a relative change of Σ_n with respect to the previous iteration of less than 1%, considering the L^∞ norm (max vector norm).

C. High resolution instantaneous reconstruction

The result of the iterative modal decomposition is a set of $rk(U'_{LR})$ orthogonal modes, ranked by their energy contribution, that provide a statistical representation of U'_{HR} after accounting for its sparsity. A representation of the instantaneous velocity field on a Cartesian grid of spacing h_{HR}, U_{HR}, may be obtained by a combination of the time-averaged flow field obtained via ensemble-averaging of the particle tracks, $\bar{U}_{HR}$, and the contribution of r dominant modes, as illustrated in Fig. 4, which may be written as

$$U_{HR} = \bar{U}_{HR} + \sum_{i=1}^{r} \psi_i \sigma_i \phi_i. \tag{4}$$

The resulting flow field is the void of gaps irrespective of the choice of h_{HR} and r, but the means for setting both coefficients will be discussed in the remainder of the document.

D. Computational complexity

The current implementation of IMR is memory demanding. While for 3D fluid mechanics problems, where the number of spatial elements is usually much bigger than the number of time realizations, the current norm for POD implementation is the so-called snapshot POD strategy (Sirovich, 1987), IMR requires storing the entire U'_{HR} data matrix for minimal overhead, to be used in the projection steps. However, for very sparse matrices, the requirements can be simplified using sparse indexing. Alternative implementations of the method could load batches of the data matrix on demand at the cost of computational time.

On the other hand, the evaluation of the computational cost is relatively simple. The dominant term is the projection (and reprojection) step, a matrix multiplication. For Eq. (2), a standard implementation of the operation would have a cost $\mathcal{O}\left(rk(U'_{LR}) \cdot n_{time} \cdot n_s^{HR}\right)$, although more advanced algorithms do exist. Since the process is repeated during n iterations until convergence, the total cost reads $\mathcal{O}\left(rk(U'_{LR}) \cdot n_{time} \cdot n_s^{HR} \cdot n\right)$. A simple trick for further time reduction is to compute only a subset of modes, n_m, with $n_m < rk(U'_{LR})$, thus reducing the cost to $\mathcal{O}\left(n_m \cdot n_{time} \cdot n_s^{HR} \cdot n\right)$.

The requirements of IMR for the experimental assessment case presented in Sec. III are summarized in Table I and compared to linear interpolation and the VIC# method for reference. All computations are performed in a workstation with 64 GB of installed RAM and Intel Xeon E5-1620 CPU.

The proposed algorithm is summarized as a pseudocode in Appendix A and also by the flow chart shown in Fig. 5.
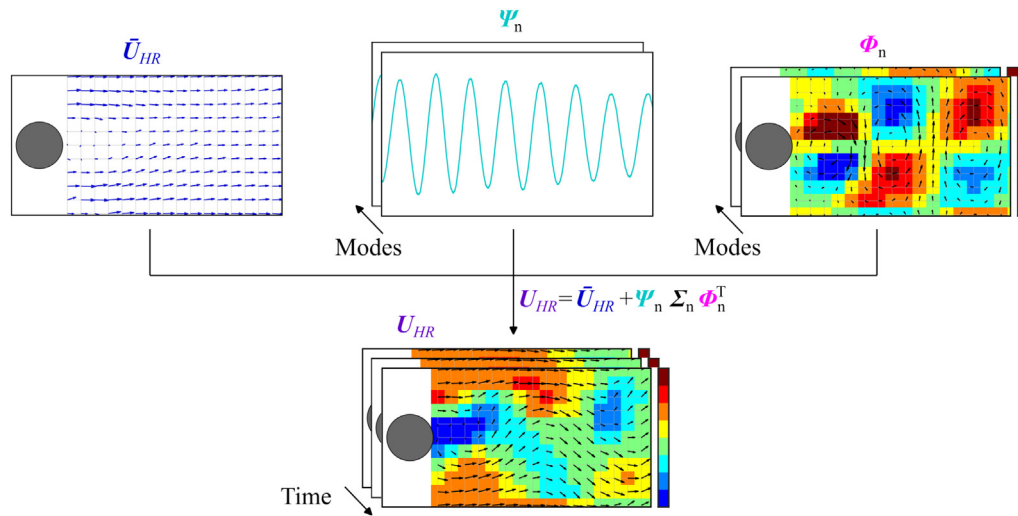
FIG. 4. Sketch of the high resolution instantaneous reconstruction. The velocity field U_{HR} is obtained by a combination of the time-averaged flow field $\bar{U}_{HR}$ and dominant IMR modes.

III. EXPERIMENTAL ASSESSMENT: CYLINDER WAKE

The experimental case considered for the evaluation of the IMR algorithm is the Kármán–Benard wake behind a circular cylinder discussed by Scarano et al. (2022). The experimental setup is described in Sec. III A. The LPT analysis is discussed in Sec. III B, followed by a description of the assessment method in Sec. III C. The flow field under study is presented in detail in Sec. III D, both in terms of instantaneous reconstruction and modal analysis.

A. Experimental apparatus and procedures

Experiments are conducted in the OJF (open jet facility), a large-scale low-speed wind tunnel at the laboratories of the aerospace engineering faculty of TU Delft. The OJF features an exit cross section of 2.85×2.85 m². A 2-m-long cylinder of diameter $D = 10$ cm is installed vertically and immersed in the free-stream flow at $U_\infty = 4$ m/s. The resulting value of the diameter-based Reynolds number is 27 000. The domain of interest is the near wake of the cylinder. The measurement covers a domain of $5D(x) \times 6D(y) \times 3D(z)$.

Neutrally buoyant, sub-millimeter helium-filled soap bubbles (HFSB) are used as tracers, produced by a seeding rake comprising 204 bubble generators, and installed ahead of the wind tunnel contraction. With the seeding rake installed, turbulence intensity in the test section is reported to increase from the nominal 0.5% of the freestream (Lignarolo et al., 2014) to approximately 0.8% (Giaquinta, 2018). After

TABLE I. Memory and CPU time requirements for the evaluation of the cylinder wake data (20 000 snapshots) using linear interpolation, VIC# and the proposed IMR method (with nine iterations until convergence).

	Memory (RAM)	CPU time
Linear interpolation	<1 GB	40 min
VIC#	2 GB	5 days
IMR	50 GB	1 h

the contraction, a seeded streamtube of an approximate diameter of 60 cm is obtained. Tracers are illuminated by two LaVision *LED-Flashlight 300* directed along the span of the cylinder. The light scattered by the tracers is recorded using three Photron *Fastcam SA 1.1* CMOS cameras (1024×1024 pixel, 12-bit, $20\,\mu$m pixel pitch) equipped with Nikon 50 mm focal length objectives, set at a numerical aperture $f_\# = 22$. The experimental setup is illustrated in Fig. 6.

A sequence of $n_{\text{time}} = 2000$ frames is obtained at $f_{acq} = 2$ kHz. Approximately eight shedding cycles are observed during the experiment, corresponding to a Strouhal number of $St = \frac{fD}{U_\infty} = 0.2$, in agreement with the literature (Williamson, 1996). Data recording and LPT processing operations are performed in the *DaVis 10* software.

B. Particle tracking analysis

The images are pre-processed with a Butterworth high-pass filter in the time domain (Sciacchitano and Scarano, 2014) to reduce background illumination. A raw-to-world mapping function is obtained by calibration with a translating target and refined with the volume self-calibration technique (Wieneke, 2008). An optical transfer function (Schanz et al., 2013) is computed prior to the evaluation of the particle images using the LPT Shake-the-Box algorithm (Schanz et al., 2016). Accepting only tracks comprising at least four consecutive samples results in an average concentration of tracks across the volume of $C = 0.12$ tracks/cm³, corresponding to an average inter-particle distance of $\bar{r} = \sqrt[3]{3/(4\pi C)} = 1.25$ cm. An illustration of particle tracks captured during ten snapshots, color-coded by streamwise velocity, is shown in Fig. 7 (left) (Multimedia view).

C. IMR assessment method

In order to evaluate the ability of the IMR method to accurately reconstruct the instantaneous flow field from sparse data, a downsampling–resampling approach has been adopted. Since the exact velocity field is unknown, a common approach in the experimental research consists of generating a reference solution from another experiment.
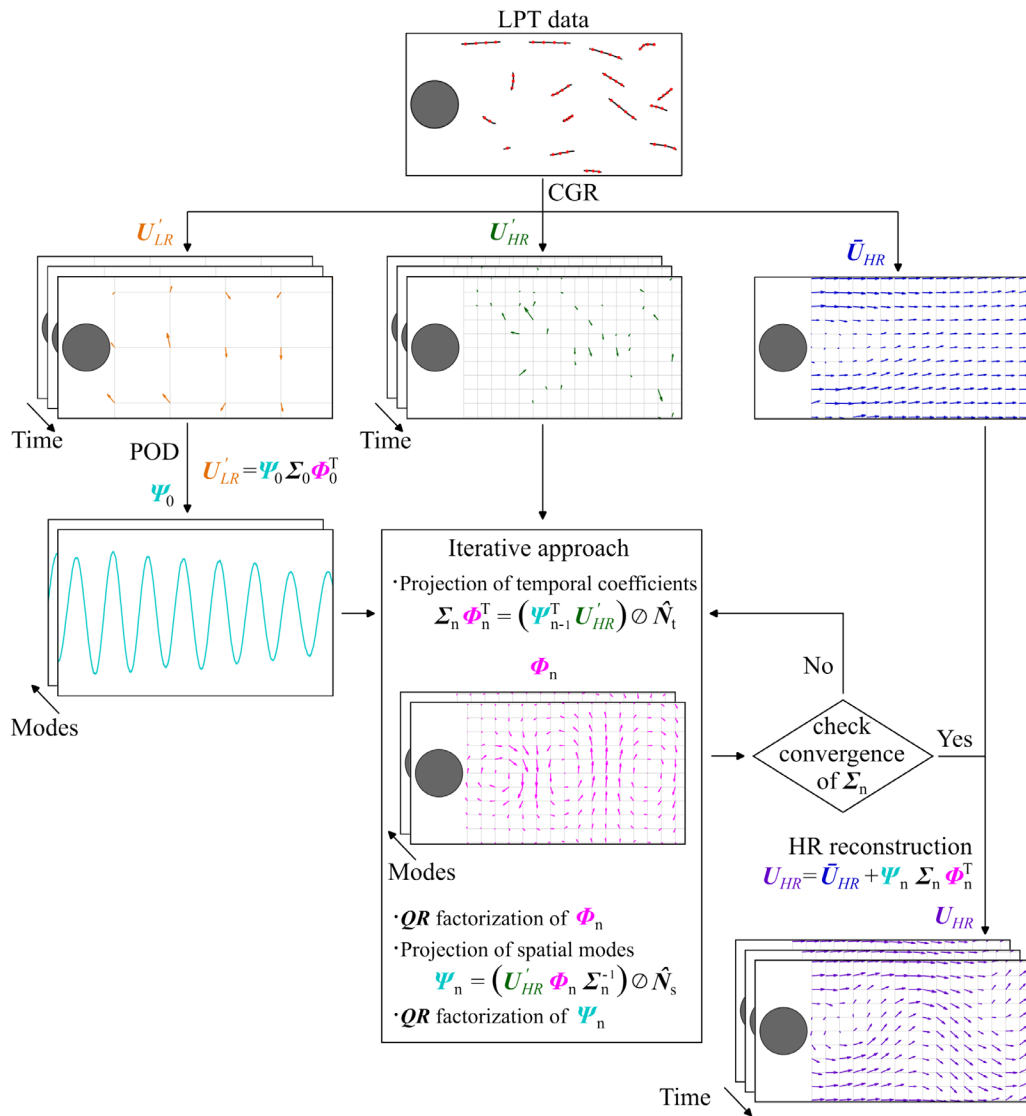
FIG. 5. Flowchart of the proposed IMR algorithm. The LPT data initially undergoes two CGR procedures at different spatial resolutions. The fluctuating component of the low-resolution version, U'_{LR}, is used to construct an initial modal decomposition using POD. The temporal modes, Ψ_0, are projected onto the sparse high resolution fluctuating velocity, U'_{HR}, to obtain a representation of the spatial modes, Φ_n, at high spatial resolution. This process is repeated until convergence of the decomposition. Finally, an instantaneous representation of the velocity field at high resolution, U_{HR}, is extracted from the time-averaged flow field $\bar{U}_{HR}$ combined with the dominant modes.

This may be done employing another experimental measurement technique (Boomsma *et al.*, 2016), the same one but at higher resolution (Sciacchitano *et al.*, 2015) or using more accurate evaluation methods (Sciacchitano *et al.*, 2013). Similarly, one may artificially downsample the data in time (Schneiders *et al.*, 2014) or space (Cai *et al.*, 2024; Schneiders and Scarano, 2016) and construct the reference solution with the full dataset. This way, a ground truth can be constructed for evaluation of a proposed methodology, while at the same time the dataset preserves the nature of the experimental measurements, including a certain level of noise or presence of outliers, for example. In the current study, the latter approach is taken for the assessment of the IMR method. The LPT dataset is artificially

coarsened by downsampling it to 1:10 of the total number of tracks. The remaining tracks are appended to the dataset, thus creating a sequence of $n_{\text{time}} = 20{,}000$ snapshots at one tenth of the original concentration, this is, $C = 0.012$ tracks/cm^3, corresponding to an average inter-particle distance of $\bar{r} = 2.7$ cm. An illustration of particle tracks at this concentration is given in Fig. 7 (right).

From the full concentration of tracks, the reference instantaneous velocity field is obtained using the VIC# algorithm (Jeon *et al.*, 2022) on a Cartesian grid with a spacing of $h = 7.3$ mm, following the criterion suggested by Schneiders and Scarano (2016), $h = \frac{1}{4}C^{-1/3}$. The resulting grid contains $n_x = 69$, $n_y = 82$, and $n_z = 41$ elements, respectively, and therefore $n_s = 695\,934$.
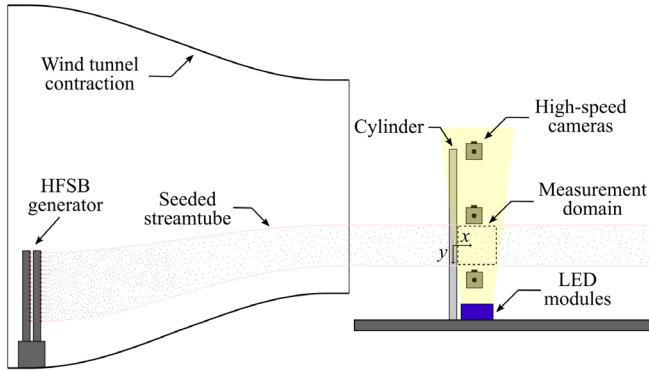
FIG. 6. Schematic side-view of the experimental setup in the OJF.

TABLE II. Main parameters of the binning procedures for the cylinder-wake dataset.

	Bin size (mm)	Overlap factor	h (mm)	n_s
Low resolution	233.6	75%	58.4	2079
High resolution	29.2	75%	7.3	695 934

From the downsampled dataset, a coarse representation of the instantaneous flow field (U_{LR}) is obtained through a binning procedure, whose parameters are summarized in Table II. Please note that $rk(U'_{LR}) = \min(n_{time}, n_s^{LR}) = n_s^{LR}$ and therefore the total number of available IMR modes is dictated by the number of spatial elements. Since the goal is to obtain a high-resolution representation of the flow field, comparable to the reference situation discussed in Sec. III C for the original LPT dataset, the target resolution for IMR is set equal to that of the reference. This represents an eight-times increase with respect to the coarse binning operation. At this resolution, a gappy representation of the flow field (U_{HR}) is obtained through a binning process summarized in Table II. The time-averaged velocity field at this spatial resolution ($\bar{U}_{HR}$) is obtained from the ensemble-average of particle tracks by fitting a second-order polynomial inside each bin (Agüera *et al.*, 2016).

D. Reference instantaneous reconstruction and modal decomposition

As discussed in Sec. III C, the reference solution is obtained from the full concentration of trajectories using the VIC# data assimilation algorithm. An instantaneous representation of the three-dimensional flow field is shown in Fig. 8 (Multimedia view) using isosurfaces of vorticity, color coded by their sign and component. The illustration reveals the dominant spanwise-coherent vortices (Kármán street), visualized through isosurfaces of spanwise vorticity ω_y (red and blue), that are shed with an alternating sign. The two-dimensional
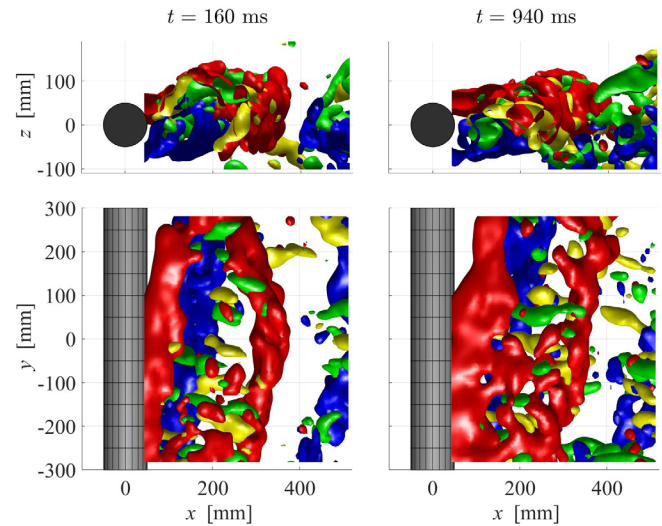

FIG. 8. Instantaneous visualization of the three-dimensional flow field using isosurfaces of spanwise (red and blue, $\omega_y = \pm70$ s^{-1}) and streamwise (green and yellow, $\omega_x = \pm70$ s^{-1}) vorticity, obtained using the VIC# algorithm. Represented both using side (upper row) and top (bottom row) views, for two different time instants: $t = 160$ ms (left) and $t = 940$ ms (right). Multimedia available online.

homogeneity of the flow is altered in several ways, as abundantly reported in the literature (Williamson, 1996). The main rollers may feature locally and occasionally an oblique orientation to the cylinder axis (oblique shedding, Prasad and Williamson, 1997; Szepessy and Bearman, 1992). Furthermore, the rollers may exhibit undulations of wavelength several times larger than the cylinder diameter, similar to the reported *mode A* exhibited in the laminar shedding regime (Williamson, 1996). Finally, thin, elongated structures interconnecting the main rollers are often observed and visualized through the dominant vorticity component ω_x (green and yellow). These structures,
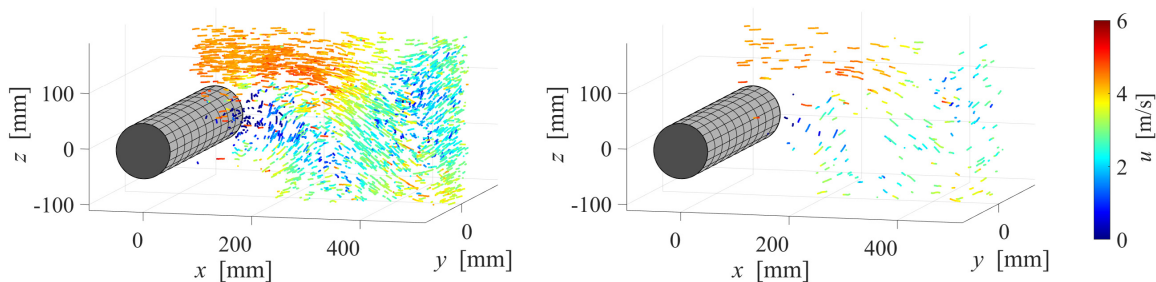

FIG. 7. Visualization of particle tracks reconstructed with Shake-the-Box (left) and coarsened measurement (only 10% of the data are retained). Tracks including 10 frames are color-coded by streamwise velocity. Only a slab of 10 cm depth is shown for clarity. Multimedia available online.
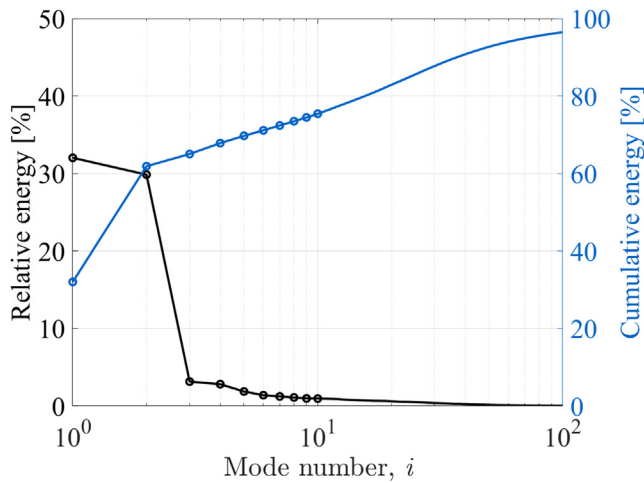
FIG. 9. Relative and cumulative modal energy contributions of the hundred most dominant modes obtained from the POD decomposition of the reference velocity field.

usually referred to as *fingers* or *ribs*, have been mostly visualized at the Reynolds number on the order of $Re = 10^2$–10^3 (Mode B, Kanaris *et al.*, 2011; Prasad and Williamson, 1997; and Williamson, 1996), while their coherence is reported to decrease with an increasing Reynolds number (Parnaudeau *et al.*, 2008), although still present up to $Re = 5000$ (Scarano and Poelma, 2009).

The instantaneous flow visualization is provided for two different time instants to illustrate the changes in the spanwise coherence of the main vortices. Inspection of Fig. 8 (right) reveals a condition whereby the main rollers are shed at an angle with respect to the cylinder. Figure 8 (left), instead, shows evident undulation of the rollers. In both examples, the rollers feature strong local distortions from the inception of the fingers.
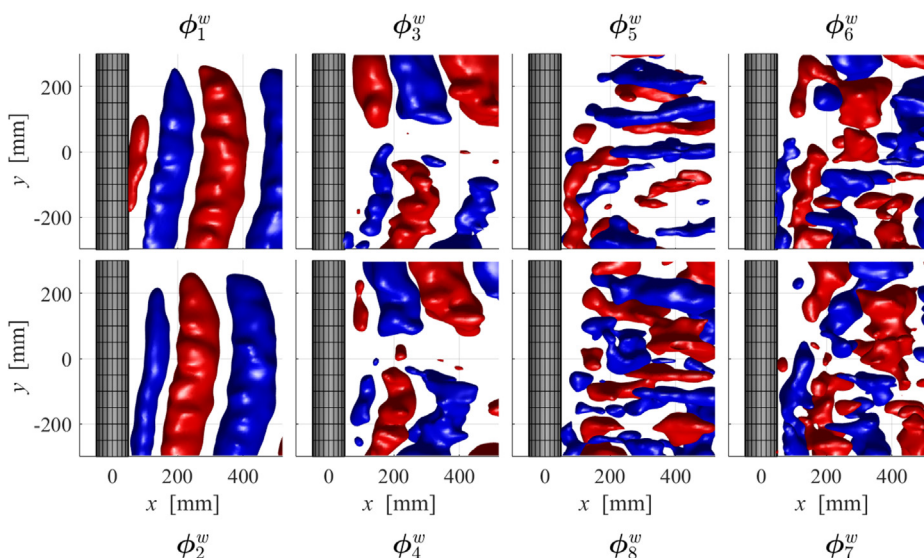
The interpretation of the flow field is further elucidated by the analysis of the POD decomposition of the reference velocity field, which will later also serve as a reference evaluating the results obtained with the IMR technique. The decomposition is summarized by the spectrum of energy captured in each mode given in Fig. 9, alongside the cumulative energy; the three-dimensional representation of the eight most dominant spatial modes shown in Fig. 10, and the corresponding temporal coefficients, given in Fig. 11 together with their frequency spectra. To the authors' best knowledge, only a handful of publications (namely, the simulations of Ma and Karniadakis, (2002), for $Re_D = 185$, and Wang *et al.*, (2012), for $Re_D = 1000$) provide a three-dimensional representation and interpretation of cylinder wake modes. In the following, we tackle the fully turbulent regime ($Re_D = 27\,000$) and extensively discuss not only the dominant Kármán wake modes (namely, modes 1 and 2), representing the advection of spanwise-coherent vortical structures, but also higher-order ones (spanwise distributed, like mode-A and with the introduction of streamwise-binormal vorticity, like mode-B), inherently three-dimensional.

The modal energy distribution returns the first two modes accounting for approximately 60% of the total turbulent kinetic energy, in agreement with existing two-dimensional experiments performed at a comparable Reynolds number (Zhang *et al.*, 2014). These two modes capture the most global feature of the Kármán wake. Because the vortex street is convected, such as a traveling wave homogeneously along the span, this first fluid dynamic mode requires two POD entries phase-shifted of a quarter wavelength ($\pi/4$). The spatial arrangement of the modes corroborates the oblique shedding discussed above, and the frequency spectra of the temporal coefficients confirm that the vortices are shed at $St = 0.2$.

POD entries 3 and 4 also exhibit a similar level of energy. Furthermore, their pattern is very similar and shifted of $\pi/4$, which is a strong indication that these two entries form an additional convective mode. In this case, the spatial distribution is not homogeneous along the span. Instead, a phase jump is exhibited, whereby the transverse motions invert their sign. The spatial arrangement of these modes
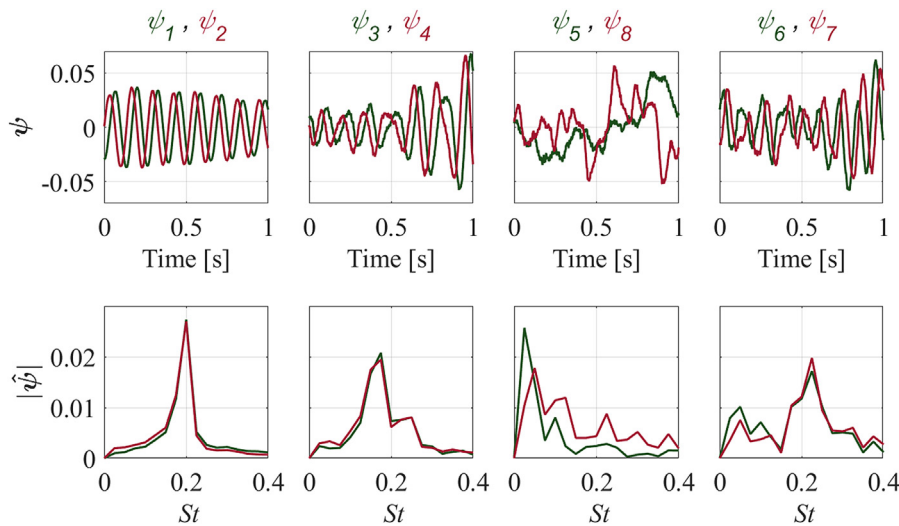

FIG. 10. Top view of the eight most dominant spatial POD modes obtained from the reference velocity field, represented using isosurfaces of ϕ^w (positive and negative, red and blue, respectively).

10 July 2024 10:52:19

FIG. 11. Representation of the eight most dominant temporal POD modes obtained from the reference velocity field, together with their frequency spectra.

suggests the presence of a spanwise wavelength, λ_y, that exceeds the measurement domain, such that $\frac{\lambda_y}{D} > 6$. In addition, the spectra of the associated temporal coefficients also reveal a peak around $St = 0.2$, indicating that these entries are still related to the Kármán street.

Mode 5 represents that part of flow motions where spanwise vorticity has been largely tilted along the streamwise direction and stretched under the action of the two counter-rotating rollers. These structures are frequently observed in Kármán wakes at higher values of the Reynolds number and feature a pattern and wavelength resembling *mode B* of the transitional cylinder wake, characterized by $\frac{\lambda_y}{D} \approx 1$ (Williamson, 1996), which is in agreement with the current observations. Also, this mode is expected to convect alongside the main rollers and it is expected that two POD entries, with similar phase shift to the above, compose this fluid-dynamic motion. However, the energy captured by this mode is similar to that of modes 6 and 7, and the mode ranking by energy becomes no guarantee that subsequently ranked POD entries pertain to the same fluid dynamic mode. Instead, mode 5 shows a stronger resemblance with mode 8, both in terms of spatial arrangement and spectra of temporal coefficients, and are therefore represented together. These entries do not show a clear phase correlation with a shift of $\pi/4$, arguably due to the fact that in the turbulent regime, the *ribs* occurrence is less regular and they may require more POD entries to fully capture their motions. Furthermore, their spectra are dominated by lower frequencies, requiring a longer time sequence for further evaluation of this phenomenon.

Instead, modes 6 and 7 form another convective pair associated with the main rollers, in this case introducing a non-homogeneity along the span governed by $\frac{\lambda_y}{D} \approx 4$, similar to what is reported in the literature for *mode A* (Williamson, 1996). As for previous entries, the peak of the spectra around $St = 0.2$ links them to the main rollers.

IV. RESULTS

The proposed IMR method is applied to the downsampled LPT dataset. The role of the number of spatiotemporal occurrences is illustrated in Sec. IV A. The resulting decomposition, compared to that obtained from the reference dataset and the DEPTV method, is discussed in Sec. IV B. Section IV C covers the instantaneous high-

resolution reconstruction of the flow field, and finally Sec. IV D discusses the statistical convergence of the proposed methodology.

A. Number of spatiotemporal occurrences

One of the key aspects of the IMR algorithm is the normalization introduced in the projection (and reprojection) step, which accounts for the changes in the seeding concentration in time and space, inherent to experimental LPT approaches. For the current dataset, changes across the measurement volume are significant. The normalized vector of temporal occurrences, $\widehat{n}_t$, is shown in Fig. 12 (left) at the mid-span of the domain ($y = 0$ mm), indicating a higher concentration of trajectories closer to the cameras (positive z).

On the other hand, only minor changes in the number of spatial occurrences are observed (continuous seeding), as shown in Fig. 12 (right). Significant drops in $\widehat{n}_s$ are only present in the initialization step of the Shake-the-Box algorithm, which propagates through the ten stacked sequences of the downsampled dataset. On average, almost 80% of the spatial bins contain no velocity information, an unprecedented value when making use of modal analysis for flow reconstruction (Raben *et al.*, 2012; Venturi and Karniadakis, 2004).

B. Modal decomposition

The modal decomposition obtained with IMR is compared to that obtained from the coarse binning operation summarized in Table II and the reconstruction from DEPTV. Furthermore, the results are benchmarked against the reference (Sec. III D). The modal energy contribution (squared elements of Σ normalized by $n_{\text{time}}n_s$ to provide a grid-independent estimation) is shown in Fig. 13 for the first hundred modes. The spatial modulation introduced in the binning operation causes an overall energy drop with respect to the reference data. The energy is largely recovered by DEPTV for the first twenty modes. After that, the lack of statistical convergence and the presence of experimental noise contaminate the modal distribution and the DEPTV solution shows a flatter decay (Cortina-Fernández *et al.*, 2021), unable to reproduce the filtering effect introduced by the VIC# methodology. The iterative approach of IMR yields an energy distribution in agreement with
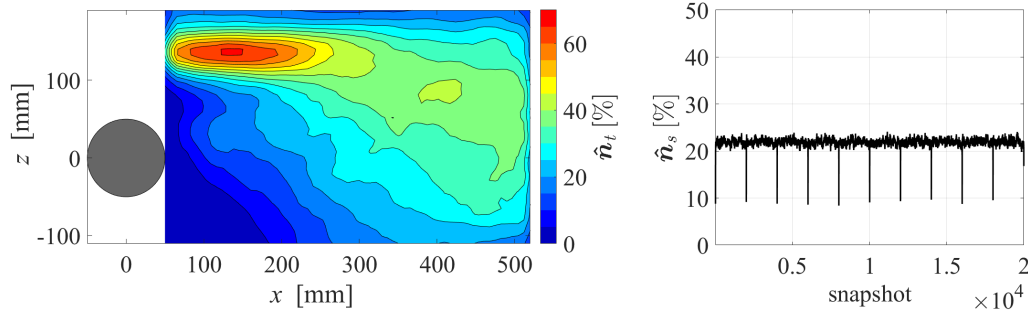
FIG. 12. Number of normalized temporal occurrences, $\hat{n}_t$, at the mid-span of the domain (left) and number of normalized spatial occurrences, $\hat{n}_s$ (right).

the reference data for the first four modes. After that, it progressively overestimates the contribution of high-order ones. As discussed in the following, this results from the appearance of high-frequency noise in the DEPTV and IMR spatial modes. For DEPTV, the added energy arising from noise is compensated by the poor reconstruction of the temporal coefficients, thus yielding an energy distribution that agrees better with the reference.

The high-resolution spatial modes obtained with the proposed methodology are compared to the other methods as shown in Fig. 14. The visualization represents one entry of the four most dominant mode pairs discussed in Sec. III D, drawn using isosurfaces (positive and negative, in red and blue, respectively) of the vertical (z) component of the spatial modes, ϕ^w. The spatial averaging introduced by the binning process is now evident when looking at modes 1 and 3. For modes 5 and 6, the output of the binning method falls below the threshold chosen for representation. The DEPTV and IMR show similar patterns, both in good agreement with the reference data. A degree of granularity (high-frequency noise) is observed for all modes. While Cortina-Fernández et al. (2021) suggest the use of a low-pass filter to counter this effect for DEPTV, the approach has not been pursued, in the absence of a theoretical justification for it.
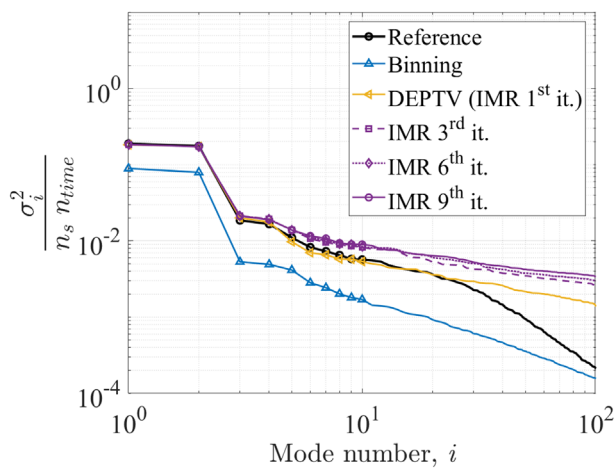

FIG. 13. Comparison of the grid-independent modal energy contribution of the hundred most dominant modes obtained from the reference POD decomposition, the coarse binning operation, DEPTV and IMR.

Regarding the modal decomposition, the main upgrade of IMR consists of providing an updated representation of the temporal modes after the computation of spatial modes at higher resolution. The effect is illustrated in Fig. 15 by comparing four dominant temporal modes with those extracted from the other methods. As expected, no significant differences are observed for modes 1 and 3, since these are well represented by the binning procedure already. However, higher-order modes are not resolved with binning and therefore depart from the reference ones. Instead, the iterative procedure of IMR is able to recover the main shape of the temporal coefficients, thus providing a significant upgrade for the use of modal decomposition as a tool for instantaneous high-resolution reconstruction. The good agreement of the temporal coefficients, combined with the granularity of the spatial modes discussed above, is argued to be responsible for the overestimate in modal energy contribution observed in Fig. 13 for IMR.

The comparison of temporal coefficients is extended to higher-order ones by computing the zero-lag cross correlation coefficient with respect to the reference modes, as a means to indicate the degree of correlation that IMR can recover. The results are given in Fig. 16 for the hundred most dominant modes. For DEPTV, the trend decays sharply after the first four modes, which could already be observed in Fig. 15. The iterative process allows us to recover agreement with the reference for modes that were not resolved by the coarse binning procedure, thus suggesting the possibility of building a more accurate reduced order model by involving more modes in the reconstruction.

C. High-resolution instantaneous reconstruction

An instantaneous high-resolution reconstruction of the flow field can be built using the IMR decomposition, as discussed in Eq. (4), by choosing a number of dominant modes r. The obtained velocity field is compared, relative to the reference dataset, to that obtained using linear interpolation from the scattered trajectories, the physics-based VIC# approach (also obtained from the downsampled set of tracks, not to be confused with the reference solution) and the DEPTV method. In every case, the target spatial resolution is set to $h = 7.3$ mm. For VIC#, the criterion $h = \frac{1}{4}C^{-1/3}$ is no longer verified. For every situation, a mean reconstruction error, ε, is built from the difference between the reconstructed velocity field, $U(x, t)$, and the reference solution, $U_{ref}(x, t)$, as

FIG. 14. Comparison of grid-independent four dominant spatial modes obtained from the reference POD decomposition, the coarse binning operation, DEPTV, and IMR. Three-dimensional visualization drawn using isosurfaces of ϕ^w (positive and negative, red and blue, respectively).
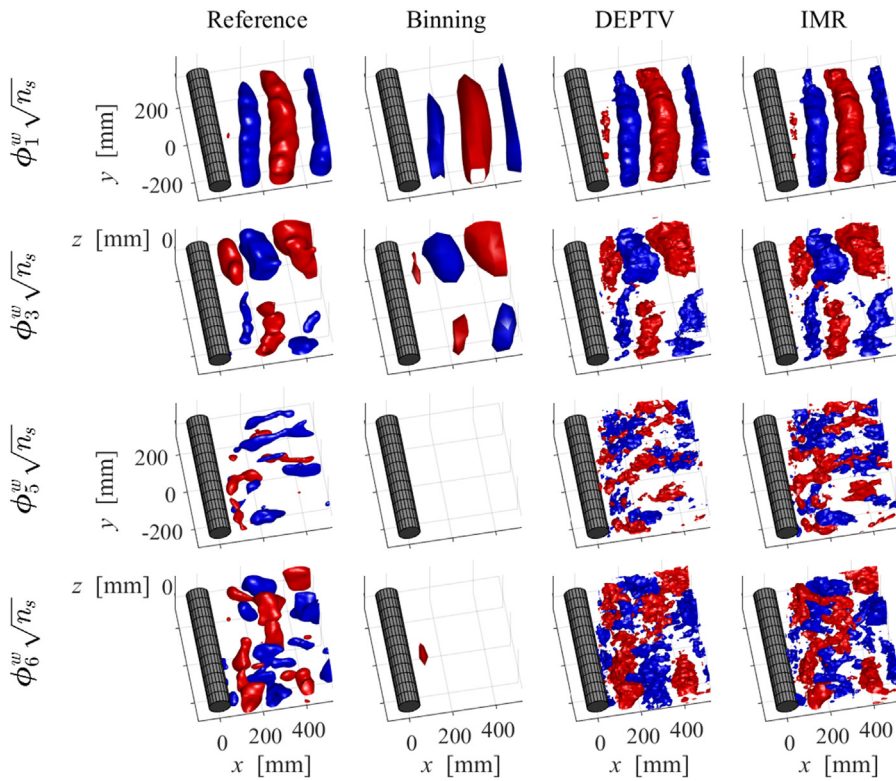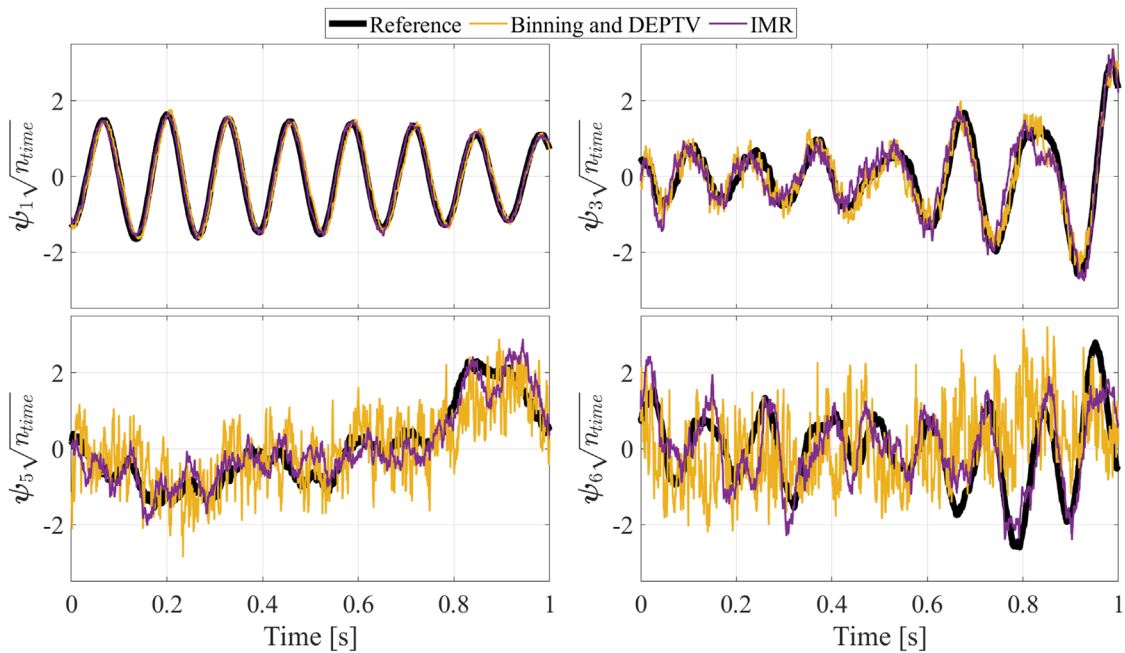

FIG. 15. Comparison of grid-independent four dominant temporal modes obtained from the reference POD decomposition, the coarse binning operation, DEPTV and IMR.
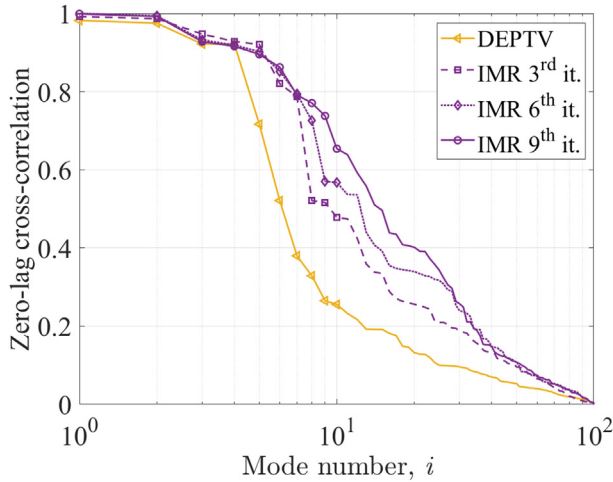
FIG. 16. Zero-lag cross correlation coefficient of the hundred most dominant DEPTV and IMR temporal modes with respect to the reference ones.

$$\varepsilon = \frac{1}{U_\infty} \sqrt{\frac{1}{n_{\text{time}} n_s^{HR}} \sum_{i=1}^{n_t} \sum_{j=1}^{n_s^{HR}} \left\| U(x_j, t_i) - U_{ref}(x_j, t_i) \right\|_2}. \quad (5)$$

For the sake of simplicity, only the first sequence of $n_{\text{time}} = 2000$ snapshots is considered in the remainder. The mean reconstruction error obtained with every data assimilation approach is shown in Fig. 17, in terms of the number of modes considered for the DEPTV and IMR algorithms. While the modal-based methods show an error decrease when compared to linear interpolation and VIC#, the relative differences are minor with respect to the error relative to the reference. For both methods, the reconstruction error initially decreases when
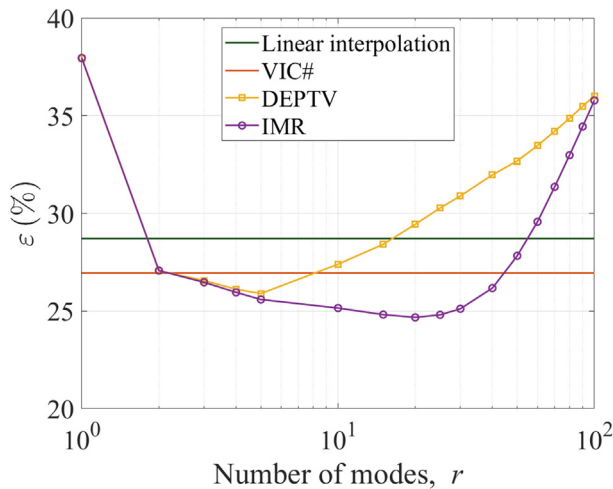

FIG. 17. Mean reconstruction error with respect to the reference velocity field, obtained using linear interpolation, VIC#, DEPTV, and IMR. For the modal-based approaches, the result is given in terms of the number of dominant modes used in the reconstruction.

considering more modes in the reconstruction since this involves a more detailed representation of the flow field. At a certain point, a minimum error is reached, after which the error increases due to the excessive presence of noise in higher-order modes. For IMR, the minimum is achieved when considering more modes than for DEPTV, a direct consequence of the better representation of the temporal modes achieved with the proposed methodology, as discussed in Sec. IV B.

To provide further insight into the reconstruction process, the streamwise spectra of vertical velocity, E_x^{ww}, are obtained for every method. The spectra, represented in terms of the streamwise wavenumber $\kappa_x = \frac{2\pi}{\lambda_x}$, where λ_x represents a streamwise wavelength, are averaged over the span and time for convergence. The results, shown in Fig. 18 (left), have been compensated using the square of the wavenumber to magnify the behavior of the medium and small scales. For DEPTV and IMR, the number of dominant modes used for the reconstruction are chosen from the minimum mean error shown in Fig. 17 (five and twenty modes, respectively). The reference spectrum is dominated by the streamwise spacing between spanwise-coherent rollers and harmonics. While the linear interpolation solution underestimates the content of the dominant large scales, the VIC# one shows the opposite trend. For both situations, the poor representation of dominant scales may be responsible for the higher mean reconstruction error. The DEPTV method captures the first peak of the spectrum at $\kappa_x = 27$ m^{-1} rather accurately since the main rollers are mostly described by the first two modes (see Fig. 14). Beyond that point, the spectrum shows a strong decay, arguably due to the fact that medium scales are contained in higher-order modes. By including more modes in the reconstruction, the IMR solution shows a much better agreement with the reference up to $\kappa_x \sim 100$ m^{-1}. However, the high-frequency noise that could already be observed in the shape of the spatial modes introduces an overestimation of the small-scale content.

The role of the number of dominant modes used in the IMR reconstruction is further illustrated in Fig. 18 (right), by showing the spectra obtained changing this parameter. As expected, choosing a small number of modes causes an underestimation of the medium-scale content. While the best agreement with the reference, up to $\kappa_x \sim 100$ m^{-1}, is obtained when considering thirty modes, the added small-scale contribution results in a slightly weaker reconstruction in terms of the mean error (see Fig. 17).

The possibility of having a reference dataset to select the dominant number of modes for the reconstruction is typically not available for experimental measurements. The appropriate choice of this parameter has been a topic of research since the introduction of modal analysis for building reduced order models, and dates back to the classic *scree test plot* (Cattell, 1966) method of finding an elbow in the modal energy distribution (as the ones showed in Fig. 13). More accurate methods have been also proposed (Gavish and Donoho, 2014), even some tailored to experimental PIV data (Epps and Krivitzky, 2019; Raiola *et al.*, 2015), but cannot be directly applied to IMR since the method does not involve a canonical POD decomposition of the experimental data. A more robust approach, purely based on the topology of the spatial modes, has been proposed by Brindise and Vlachos (2017) and is suggested as suitable for the implementation of IMR. The method targets the spatial differences between modes containing relevant flow structures and those corrupted by random noise. It is implemented via calculation of the Shannon entropy of the spatial
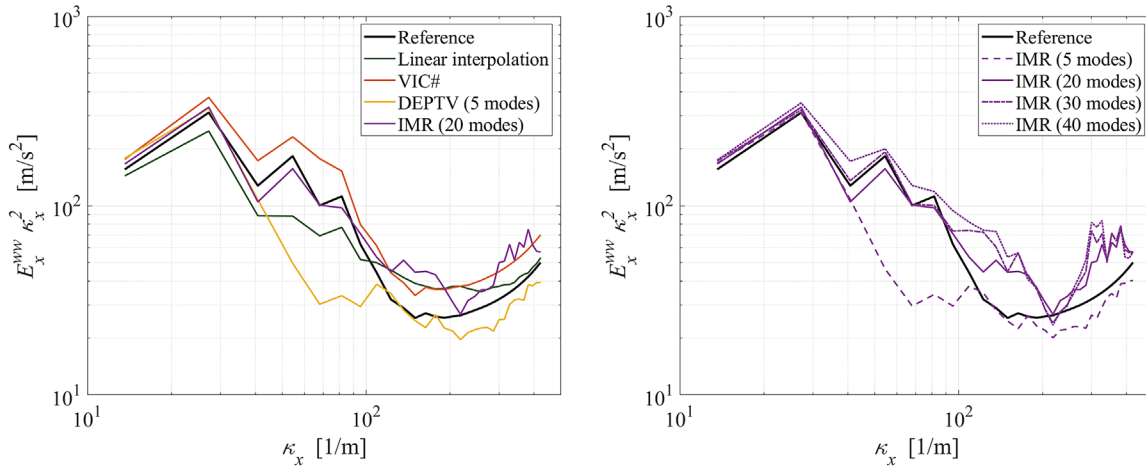
FIG. 18. Compensated streamwise spectra of vertical velocity, averaged in time and over the span, for different data assimilation methods (left) and obtained with IMR changing the number of dominant modes used in the reconstruction (right).

modes after a change of basis using the discrete cosine transform. Extending the procedure described by Brindise and Vlachos (2017) to a three-dimensional situation returns an optimum threshold of nineteen modes, in excellent agreement with the error-based minimization with respect to the reference dataset discussed in Fig. 17.

FIG. 19. Instantaneous visualization of the three-dimensional flow field using isosurfaces of spanwise (red and blue, $\omega_y = \pm 70$ s^{-1}) and streamwise (green and yellow, $\omega_x = \pm 70$ s^{-1}) vorticity, for the reference solution (top-left), linear interpolation (top-right), the VIC# algorithm (bottom-left) and IMR with $r = 19$ (bottom-right). Multimedia available online.

The topology of the reconstructed flow field may be inspected in Fig. 19 (Multimedia view). A comparison is made between the reference solution, linear interpolation, the VIC# algorithm and a reconstruction using IMR with $r = 19$. The visualization shows isosurfaces of spanwise vorticity, $\omega_y = \pm 70$ s^{-1} (red and blue), and also isosurfaces of streamwise vorticity, $\omega_x = \pm 70$ s^{-1} (green and yellow). The interpretation of the instantaneous organization of the flow field, from the reference solution, has already been discussed in Sec. III D. Linear interpolation fails to represent the shear layers and most of the streamwise-oriented vortical structures. In general, the solution is strongly affected by the spatial differentiation operator required for the visualization of the vorticity field. The VIC# algorithm produces a solution that appears contaminated by the presence of small structures, arguably due to the fact that the grid resolution has been chosen beyond the presence of particle trajectories, causing an ill-posed minimization problem. The IMR reconstruction shows better agreement with the reference, but certain features are worth being discussed. While the vorticity in the shear layers and the main rollers are accurately reconstructed, some of the *ribs* (green and yellow structures) do not appear in the reconstructed flow field (especially for $x > 400$ mm), likely because their representation involves higher-order modes. On the other hand, some structures are introduced that do not find a correspondence in the reference case (around $x = 300$ and $y = 200$ mm), arguably because they do appear in other shedding cycles of the full acquisition. In general, this situation highlights the capabilities of IMR in reconstructing instantaneous vortical structures that are not accurately sampled by the particle trajectories but at the same time the difficulty of dealing with certain turbulent events for which providing a statistical description is challenging.
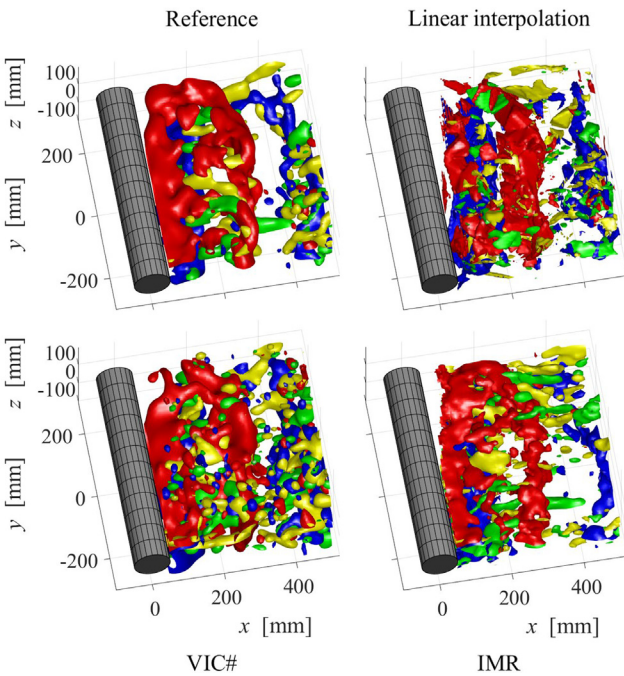
D. Statistical convergence of the IMR method

As for any modal-based reconstruction method, IMR relies on the statistical convergence of a series of flow events, represented by modes, with high-energy modes typically requiring less instantaneous realizations to converge. As discussed in Sec. III C, the IMR method

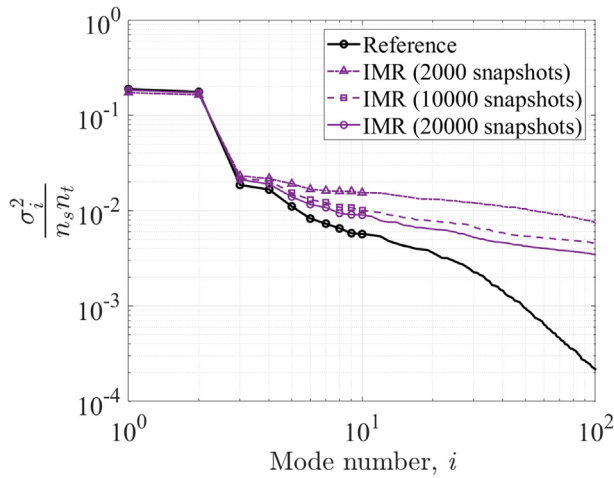**FIG. 20.** Comparison of the grid-independent modal energy contribution of the first 100 POD modes obtained from the reference POD decomposition and the IMR method applied to $n_{time} = 2000$, $n_{time} = 10\,000$, and $n_{time} = 20\,000$ snapshots.

has been applied to a downsampled version of the LPT dataset, producing ten stacked sequences of $n_{time} = 2000$ snapshots each. The obtained modal decomposition and instantaneous reconstruction are compared here to those extracted from considering only a subset of the total number of snapshots available.

The modal energy distributions are shown in Fig. 20, obtained from the POD decomposition of the reference flow field and the IMR method applied to $n_{time} = 2000$, $n_{time} = 10\,000$, and $n_{time} = 20\,000$ snapshots. As expected, using more snapshots reduces the discrepancy with respect to the reference. The first two modes converge rather well, while the discrepancy increases for higher-order ones. After approximately mode number ten, the three IMR curves show a parallel trend,

as dictated by the noise level of the experimental dataset (Cortina-Fernández *et al.*, 2021).

The effect of the number of snapshots in the reconstructed velocity field is studied by comparing the mean reconstruction error with respect to the reference, shown in Fig. 21 (left), and the time- and spanwise-averaged streamwise spectra of vertical velocity, shown in Fig. 21 (right). The mean error trends demonstrate that improving the statistical convergence of the decomposition allows not only reducing the global error but also makes it possible to include more modes in the reconstruction before they become too much affected by random noise. The latter is confirmed by looking at the spectra, obtained using $r = 20$ for every situation. For the case $n_{time} = 2000$ snapshots, a strong overestimation of the medium and small-scale contributions is observed, direct consequence of the presence of noise in some of the modes employed for the reconstruction.

The analysis of the statistical convergence of IMR highlights one of the main limitations of the proposed methodology, which is inherent to experimental time-resolved measurements. The sequence of $n_{time} = 2000$ snapshots considered in this study does only capture approximately eight shedding cycles (see Fig. 15). While the high acquisition frequency is necessary for particle tracking, the resulting snapshots are strongly correlated (Sciacchitano and Wieneke, 2016). For modal-based reconstruction methods, it is advisable to collect more than one sequence of time-resolved information for improved statistical convergence. This will especially affect higher-order modes and would make possible extending the IMR method to spectrally richer flows.

V. CONCLUSIONS

A method has been proposed for the dense reconstruction of the three-dimensional velocity field from sparse measurements obtained with LPT. The IMR technique leverages upon the principle of proper orthogonal decomposition in a similar way as introduced recently with DEPTV. However, attention is placed on the consistency of the temporal coefficients, alongside that of the spatial modes. This result is
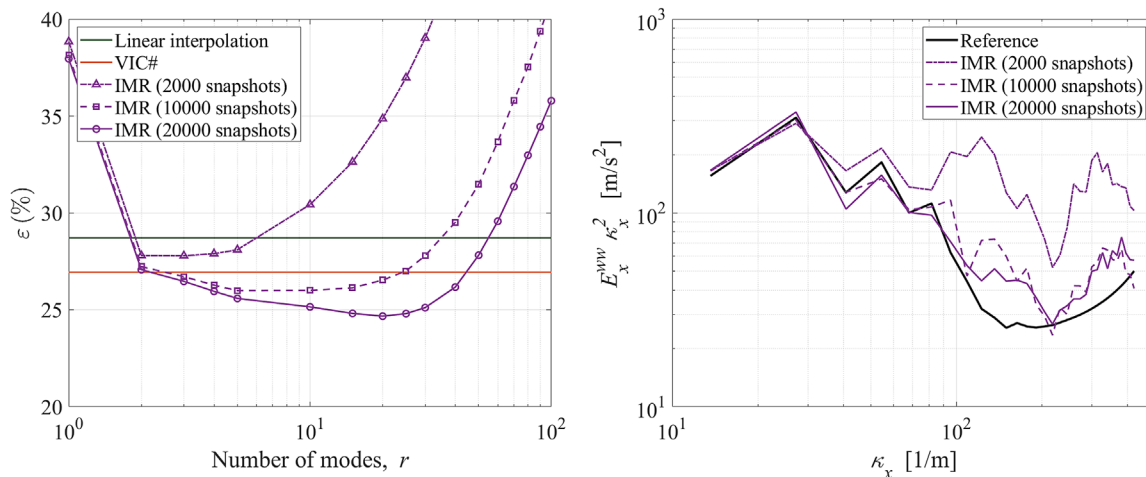
FIG. 21. Mean reconstruction error with respect to the reference velocity field, obtained using linear interpolation, VIC# and IMR applied to $n_{time} = 2000$, $n_{time} = 10\,000$, and $n_{time} = 20\,000$ snapshots (left). Compensated streamwise spectra of vertical velocity, averaged in time and over the span, for the reference velocity field and the IMR method applied to $n_{time} = 2000$, $n_{time} = 10\,000$, and $n_{time} = 20\,000$ snapshots (right).

obtained by iteratively projecting the initial temporal and spatial POD modes onto the measured particle velocity field. The higher level of spatial resolution is used to build a reduced order model from the dataset.

The IMR method is evaluated on experimental data obtained in the turbulent wake of a circular cylinder and a comparison is afforded with existing approaches, based on linear interpolation, local averaging (binning), and data assimilation (VIC#). Furthermore, the method is compared to the existing modal-based DEPTV method. The data are artificially coarsened by sub-sampling the particle tracers, such as to yield a low-concentration measurement, to compare all methods, whereas the data at the original higher resolution is used to provide a reference.

The spatial modes obtained using IMR follow with good fidelity the reference data for the first 8 entries and cumulative energy of 75%. Furthermore, the phase relations between pairs contributing to the same fluid dynamic mode are more clearly restored with the IMR algorithm, compared to DEPTV. This condition entitles to a robust interpretation of the modes and their combination into pairs, when dealing with convective instabilities. In addition, the iterative approach allows recovering the shape of the temporal coefficients that were not captured by the initial window-based averaging approach. This shows that IMR has potential to recover information at spatial scales comparable to the inter-particle distance of the LPT dataset.

A reduced order model is built using the first 20 modes, yielding with clarity the main motions exhibited in the unsteady flow and in good agreement with the reference high-resolution data. The obtained flow field shows that IMR can correctly model the shear layers on both sides of the cylinder, the main spanwise-coherent shed vortices, and also the smaller streamwise-oriented structures interconnecting those. In general, the method outperforms the state-of-the-art data assimilation methodologies in terms of reconstruction error, spatial spectra, and coherence of the reconstruction. Future works will explore the applicability of the method to other flow problems featuring a broader distribution of the modal energy.

AUTHOR DECLARATIONS

Conflict of Interest

The authors have no conflicts to disclose.

Author Contributions

Adrian Grille Guerra: Conceptualization (equal); Data curation (equal); Investigation (equal); Methodology (equal); Software (equal); Validation (equal); Visualization (equal); Writing – original draft (equal). **Andrea Sciacchitano:** Conceptualization (equal); Funding acquisition (equal); Project administration (equal); Resources (equal); Supervision (equal); Writing – review & editing (equal). **Fulvio Scarano:** Conceptualization (equal); Funding acquisition (equal); Project administration (equal); Resources (equal); Supervision (equal); Writing – review & editing (equal).

DATA AVAILABILITY

The data that support the findings of this study are openly available in 4TU at http://doi.org/10.4121/caa059d2-7657–4301-a805-767e9ca98eab (Grill Guerra et al., 2024).

APPENDIX: IMR PSEUDOCODE

```
1)   % IMR pseudocode
2)   % Grille Guerra et al. (2024)
3)
4)   % Initialize CGR velocity fields
5)        U_LR = Low resolution instantaneous velocity field
6)        U_HR = High resolution instantaneous velocity field
             (gappy)
7)        Ū_HR = Time-averaged velocity field at high spatial
             resolution
8)
9)   % Perform POD decomposition of low-resolution velocity
       fluctuations
10)       Ū_LR = mean(U_LR)
11)       U'_LR = U_LR − Ū_LR
12)       [Ψ, Σ, Φ] = svd(U'_LR)
13)
14)  % Obtain high-resolution velocity fluctuations (gappy) and
       spatiotemporal occurrences
15)       U'_HR = U_HR − Ū_HR
16)       [n_s, n_time] = size(U'_HR)
17)       n_s = Count number of non-zero elements in every
             snapshot
18)       N̂_s = n_s/n_s
19)       n_t = Count number of non-zero elements in every
             grid point
20)       N̂_t = n_t/n_time
21)
22)  % Iterative approach
23)       converged = FALSE
24)       while converged == FALSE
25)             % Project temporal coefficients
                 onto high-resolution velocity
                 fluctuations
26)                   sigma_phi = (Ψ^T U'_HR) ⊘ N̂_t
27)
28)             % Calculate modal energies and sort
                 modes according to their energy
                 contribution
29)                   Σ = norm(sigma_phi)
30)                   [Σ, sorting] = sort(Σ)
31)                   sigma_phi = sigma_phi
                       (sorting)
32)
33)             % Obtain orthogonal spatial modes via
                 QR factorization
34)                   Φ = qr(sigma_phi)
35)
36)             % Update temporal coefficients from spa-
                 tial modes reprojection onto velocity
                 fluctuations
```

10 July 2024 10:52:19

37)　　　　　　　　$\boldsymbol{\Psi} = \left(\boldsymbol{U}'_{HR} \boldsymbol{\Phi} \boldsymbol{\Sigma}^{-1} \right) \oslash \widehat{\boldsymbol{N}}_s$

38)

39)　　　　　% Restore orthogonality via $\boldsymbol{QR}$ factorization

40)　　　　　　　　$\boldsymbol{\Psi} = \mathrm{qr}\left(\boldsymbol{\Psi} \right)$

41)

42)　　　　　% Check for convergence of modal energies

43)　　　　　　　if max(abs(($\boldsymbol{\Sigma}(\mathrm{k}) - \boldsymbol{\Sigma}(\mathrm{k}-1)$)))/$\boldsymbol{\Sigma}(\mathrm{k}-1)$)
　　　　　　　　　< threshold

44)　　　　　　　　　converged = TRUE

45)　　　　　　　end

46)

47)　　　　　　k = k + 1

48)　　　end

49)

50)　　% Estimate high-resolution velocity field using r dominant modes

51)　　　　$\boldsymbol{U}_{HR} = \bar{\boldsymbol{U}}_{HR} + \sum_{i=1}^{r} \boldsymbol{\psi}_i \sigma_i \boldsymbol{\phi}_i$

52)

REFERENCES

Agüera, N., Cafiero, G., Astarita, T., and Discetti, S., "Ensemble 3D PTV for high resolution turbulent statistics," Meas. Sci. Technol. **27**(12), 124011 (2016).

Boomsma, A., Bhattacharya, S., Troolin, D., Pothos, S., and Vlachos, P., "A comparative experimental evaluation of uncertainty estimation methods for two-component PIV," Meas. Sci. Technol. **27**(9), 094006 (2016).

Borée, J., "Extended proper orthogonal decomposition: A tool to analyse correlated events in turbulent flows," Exp. Fluids **35**(2), 188–192 (2003).

Bosbach, J., Kühn, M., and Wagner, C., "Large scale particle image velocimetry with helium filled soap bubbles," Exp. Fluids **46**(3), 539–547 (2009).

Brindise, M. C. and Vlachos, P. P., "Proper orthogonal decomposition truncation method for data denoising and order reduction," Exp. Fluids **58**(4), 28 (2017).

Cai, S., Gray, C., and Karniadakis, G. E., "Physics-informed neural networks enhanced particle tracking velocimetry: An example for turbulent jet flow," IEEE Trans. Instrum. Meas. **73**, 2519109 (2024).

Cattell, R. B., "The scree test for the number of factors," Multivar. Behav. Res. **1**(2), 245–276 (1966).

Cortina-Fernández, J., Sanmiguel Vila, C., Ianiro, A., and Discetti, S., "From sparse data to high-resolution fields: Ensemble particle modes as a basis for high-resolution flow characterization," Exp. Therm. Fluid Sci. **120**, 110178 (2021).

Cowen, E. A. and Monismith, S. G., "A hybrid digital particle tracking velocimetry technique," Exp. Fluids **22**(3), 199–211 (1997).

De Baar, J. H. S., Percin, M., Dwight, R. P., Van Oudheusden, B. W., and Bijl, H., "Kriging regression of PIV data using a local error estimate," Exp. Fluids **55**(1), 1650 (2014).

Eckart, C. and Young, G., "The approximation of one matrix by another of lower rank," Psychometrika **1**(3), 211–218 (1936).

Elsinga, G. E., Scarano, F., Wieneke, B., and Van Oudheusden, B. W., "Tomographic particle image velocimetry," Exp. Fluids **41**(6), 933–947 (2006).

Epps, B. P. and Krivitzky, E. M., "Singular value decomposition of noisy data: Noise filtering," Exp. Fluids **60**(8), 126 (2019).

Gavish, M. and Donoho, D. L., "The optimal hard threshold for singular values is $4/\sqrt{3}$," IEEE Trans. Inf. Theory **60**(8), 5040–5053 (2014).

Gesemann, S., "From particle tracks to velocity, acceleration and pressure fields using B-splines and penalties," in 18th International Symposium on the Application of Laser and Imaging Techniques to Fluid Mechanics, 2016.

Giaquinta, D., *The Flow Topology of the Ahmed Body in Cross-Wind* (TU Delft, 2018).

Grille Guerra, A., Sciacchitano, A., and Scarano, F. (2024), "Supporting data for: 'Iterative modal reconstruction for sparse particle tracking data,'" 4TU. Research Data. http://doi.org/10.4121/caa059d2-7657-4301-a805-767e9ca98eab

Jeon, Y. J., Müller, M., and Michaelis, D., "Fine scale reconstruction (VIC#) by implementing additional constraints and coarse-grid approximation into VIC+," Exp. Fluids **63**(4), 70 (2022).

Jeon, Y. J., Müller, M., Michaelis, D., and Wieneke, B., "Data assimilation-based flow field reconstruction from particle tracks over multiple time steps," in 13th International Symposium on Particle Image Velocimetry, 2019.

Kähler, C. J., Scharnowski, S., and Cierpka, C., "On the resolution limit of digital particle image velocimetry," Exp. Fluids **52**(6), 1629–1639 (2012).

Kanaris, N., Grigoriadis, D., and Kassinos, S., "Three dimensional flow around a circular cylinder confined in a plane channel," Phys. Fluids **23**(6), 064106 (2011).

Lignarolo, L. E. M., Ragni, D., Krishnaswami, C., Chen, Q., Simão Ferreira, C. J., and van Bussel, G. J. W., "Experimental analysis of the wake of a horizontal-axis wind-turbine model," Renewable Energy **70**, 31–46 (2014).

Ma, X. and Karniadakis, G. E., "A low-dimensional model for simulating three-dimensional cylinder flow," J. Fluid Mech. **458**, 181–190 (2002).

Mendez, M. A., Balabane, M., and Buchlin, J.-M., "Multi-scale proper orthogonal decomposition of complex fluid flows," J. Fluid Mech. **870**, 988–1036 (2019).

Parnaudeau, P., Carlier, J., Heitz, D., and Lamballais, E., "Experimental and numerical studies of the flow over a circular cylinder at Reynolds number 3900," Phys. Fluids **20**(8), 085101 (2008).

Prasad, A. and Williamson, C. H. K., "Three-dimensional effects in turbulent bluff-body wakes," J. Fluid Mech. **343**, 235–265 (1997).

Raben, S. G., Charonko, J. J., and Vlachos, P. P., "Adaptive gappy proper orthogonal decomposition for particle image velocimetry data reconstruction," Meas. Sci. Technol. **23**(2), 025303 (2012).

Raiola, M., Discetti, S., and Ianiro, A., "On PIV random error minimization with optimal POD-based low-order reconstruction," Exp. Fluids **56**(4), 75 (2015).

Scarano, F. and Poelma, C., "Three-dimensional vorticity patterns of cylinder wakes," Exp. Fluids **47**(1), 69–83 (2009).

Scarano, F., Schneiders, J. F. G., Saiz, G. G., and Sciacchitano, A., "Dense velocity reconstruction with VIC-based time-segment assimilation," Exp. Fluids **63**(6), 96 (2022).

Schanz, D., Gesemann, S., and Schröder, A., "Shake-The-Box: Lagrangian particle tracking at high particle image densities," Exp. Fluids **57**(5), 70 (2016).

Schanz, D., Gesemann, S., Schröder, A., Wieneke, B., and Novara, M., "Non-uniform optical transfer functions in particle imaging: Calibration and application to tomographic reconstruction," Meas. Sci. Technol. **24**(2), 024009 (2013).

Schneiders, J. F. G., Dwight, R. P., and Scarano, F., "Time-supersampling of 3D-PIV measurements with vortex-in-cell simulation," Exp. Fluids **55**(3), 1692 (2014).

Schneiders, J. F. G. and Scarano, F., "Dense velocity reconstruction from tomographic PTV with material derivatives," Exp. Fluids **57**(9), 139 (2016).

Schröder, A. and Schanz, D., "3D Lagrangian particle tracking in fluid mechanics," Annu. Rev. Fluid Mech. **55**(1), 511–540 (2023).

Sciacchitano, A., Neal, D. R., Smith, B. L., Warner, S. O., Vlachos, P. P., Wieneke, B., and Scarano, F., "Collaborative framework for PIV uncertainty quantification: Comparative assessment of methods," Meas. Sci. Technol. **26**(7), 074004 (2015).

Sciacchitano, A. and Scarano, F., "Elimination of PIV light reflections via a temporal high pass filter," Meas. Sci. Technol. **25**(8), 084009 (2014).

Sciacchitano, A. and Wieneke, B., "PIV uncertainty propagation," Meas. Sci. Technol. **27**(8), 084006 (2016).

Sciacchitano, A., Wieneke, B., and Scarano, F., "PIV uncertainty quantification by image matching," Meas. Sci. Technol. **24**(4), 045302 (2013).

Sirovich, L., "Turbulence and the dynamics of coherent structures. III. Dynamics and scaling," Quart. Appl. Math. **45**(3), 583–590 (1987).

Szepessy, S. and Bearman, P. W., "Aspect ratio and end plate effects on vortex shedding from a circular cylinder," J. Fluid Mech. **234**(1), 191 (1992).

Tirelli, I., Ianiro, A., and Discetti, S., "A simple trick to improve the accuracy of PIV/PTV data," Exp. Therm. Fluid Sci. **145**, 110872–110876 (2023).

Tirelli, I., Solera-Rico, A., Guemes, A., Sanmiguel Vila, C., Ianiro, A., and Discetti, S., "Assessment of data-driven 3D PTV techniques," in 15th International Symposium on Particle Image Velocimetry (ISPIV 2023) June 19–21, 2023, San Diego, California, 2023.

Van Oudheusden, B. W., "PIV-based pressure measurement," Meas. Sci. Technol. **24**(3), 032001 (2013).

Venturi, D. and Karniadakis, G. E., "Gappy data and reconstruction procedures for flow past a cylinder," J. Fluid Mech. **519**, 315–336 (2004).

Wang, Z., Akhtar, I., Borggaard, J., and Iliescu, T., "Proper orthogonal decomposition closure models for turbulent flows: A numerical comparison," Comput. Methods Appl. Mech. Eng. **237–240**, 10–26 (2012).

Wieneke, B., "Volume self-calibration for 3D particle image velocimetry," Exp. Fluids **45**(4), 549–556 (2008).

Williamson, C. H. K., "Vortex dynamics in the cylinder wake," Annu. Rev. Fluid Mech. **28**, 477–539 (1996).

Zhang, Q., Liu, Y., and Wang, S., "The identification of coherent structures using proper orthogonal decomposition and dynamic mode decomposition," J. Fluids Struct. **49**, 53–72 (2014).

10 July 2024 10:52:19